*China Ocean Eng.*, 2024, Vol. 38, No. 1, P. 68–80
DOI: https://doi.org/10.1007/s13344-024-0006-1, ISSN 0890-5487
http://www.chinaoceanengin.cn/ E-mail: coe@nhri.cn

# Energy Harvesting in the Wake of An Inverted C-Shaped Bluff Body

WANG Jun-lei[a], LI Shen-fang[a], Md. Mahbub ALAM[b], ZHU Hong-jun[c, *], HU Guo-biao[d, *]

[a] School of Mechanical and Power Engineering, Zhengzhou University, Zhengzhou 450000, China

[b] Center for Turbulence Control, Harbin Institute of Technology (Shenzhen), Shenzhen 518055, China

[c] State Key Laboratory of Oil and Gas Reservoir Geology and Exploitation, Southwest Petroleum University, Chengdu 610500, China

[d] Internet of Things Thrust, The Hong Kong University of Science and Technology (Guangzhou), Guangzhou 511400, China

Received April 18, 2023; revised August 15, 2023; accepted September 18, 2023

**Abstract**

This paper proposes a novel wake-induced vibration (WIV)-based energy harvesting system consisting of two bluff bodies. An inverted C-shaped bluff body is stationary installed at the upstream position to generate an interference wake street, and a cylinder bluff body equipped with a transducer is elastically suspended at the downstream position to harness WIV energy. The hydrodynamics and energy harvesting (EH) performance of the proposed system are investigated via experimental studies. The reduced velocity ($U^*$) ranging from 2 to 14 (the corresponding Reynolds number ranging from 15100 to 106200) is considered in the present study. It is found that the wake generated by the inverted C-shaped bluff body significantly affects the EH performance. Enlarging the opening angle ($\alpha$) of the C-shaped bluff body increases the vibration amplitude of the downstream cylinder, thereby increasing the harvested power. When the spacing ($L$) between two bluff bodies is two times the cylinder diameter ($D$), the wake-induced vibration (WIV) mode is observed, while the combined WIV and wake galloping (WG) mode occurs when $\alpha$ is 150°, and $L$ equals $3D$ or $4D$. The average drag coefficient becomes negative when $L$ is $2D$, $3D$, or $4D$. By carefully configuring a C-shaped bluff body, the wake generated by it can bring an augmenting effect on the vibration of the downstream EH cylinder. For example, the RMS power output of the proposed EH system reaches a maximum of 0.31 W at $U^* = 8$ and $L = 4D$, which is 300% greater than that of its traditional counterpart. Furthermore, after a number of case studies, it is identified that the proposed EH system can achieve the best performance when $\alpha$ is 150° and $L = 2D$.

**Key words:** wake-induced vibration, vortex-induced vibration, galloping, energy harvesting, bluff body

**Citation:** Wang, J.L., Li, S.F., Alam, M.M., Zhu, H.J., Hu, G.B., 2024. Energy harvesting in the wake of an inverted C-shaped bluff body. China Ocean Eng., 38(1): 68–80, doi: https://doi.org/10.1007/s13344-024-0006-1

## 1 Introduction

Miniaturized and low-power consumption sensors have been substantially developed and utilized in recent years with the rapid development of Micro-Electro-Mechanical Systems (MEMS) technology, which has also significantly promoted the development of the Internet of Things (IoT) (Fan et al., 2021; Zhang et al., 2019). The construction of a large-scale IoT has led to the urgent need for sustainable power supplies for millions and billions of sensors (Jiang et al., 2017; Zou et al., 2017). Many renewable energy resources such as solar, thermal, and fluidic energy, are available in the ambient environment (Sun, 2022; Tian et al., 2022; Zhao et al., 2019b). Among these sources, fluidic energy has many advantages (Li et al., 2020b; Zhao et al., 2019a, 2020a). Traditionally, hydraulic and wind turbines are often used to convert fluidic energy into electricity. Unfortunately, these devices are unsuitable for powering distributed sensor networks due to their large sizes (Chitrakar et al., 2020; Mrope et al., 2021; Peng et al., 2021). Flow-induced vibration (FIV) is a well-known structural vibration phenomenon excited by the coupling interaction between the flow and structure (Alam, 2022; Ali et al., 2021). Flow-induced vibration includes vortex-induced vibration (VIV) (Munir et al., 2021; Wang et al., 2021b), galloping (Yang et

---

Foundation item: This work was financially supported by the National Natural Science Foundation of China (Grant Nos. 51977196, 52277227, and52305135), Open Project of Henan Key Laboratory of Intelligent Manufacturing of Mechanical Equipment, Zhengzhou University of Light Industry (Grant No. IM202302), the Natural Science Foundation of Excellent Youth of Henan Province (Grant No. 222300420076), the Science and Technology Research & Development Joint Foundation of Henan Province-Young Scientists (Grant No. 225200810099), the Program for Science & Technology Innovation Talents in Universities of Henan Province (Grant No. 23HASTIT010), and the National Center for International Research of Subsea Engineering Technology and Equipment (Grant No. 3132023366) .

*Corresponding authors. E-mail: zhuhj@swpu.edu.cn; guobiaohu@hkust-gz.edu.cn

al., 2021), flutter (Elahi et al., 2020), and wake-induced vibration (WIV) (Bhatt and Alam, 2018; Qin et al., 2019; Xu et al., 2019). Over a decade's development, EH technology based on FIV has become a promising solution for powering low-power consumption MEMS.

In the last two decades, the FIV phenomenon of tandem bluff bodies has attracted research attention (Alam, 2021). Many theoretical and experimental studies have been conducted to investigate the WIV phenomenon of tandem bluff bodies and study the coupling mechanism behind this phenomenon (Chen et al., 2018; Qin et al., 2017). For example, Li et al. (2018) studied the flow characteristics of tandem cylinders. They pointed out that there exists a critical spacing ratio between two cylinders when the Reynolds number $Re = 2.2\times10^4$. When the distance between two cylinders is less than this critical value, the drag coefficient of the downstream cylinder becomes negative. If the square bluff bodies are arranged in series at $Re = 1.6\times10^4$ and $1.0\times10^6$, two critical spacing values are, respectively, identified. Again, the drag coefficient of the downstream square bluff body is less than 0 when the spacing is less than the critical value. Li et al. (2020a) studied the WIV of tandem cylinders within a high region of $Re$ (= 17000−98000). They pointed out that the downstream cylinders can exhibit different vibration characteristics, including galloping, separated vortex resonance and galloping, and vortex resonance, as the spacing between tandem cylinders varies. Zhu and Wang (2019) installed a C-shaped interference bluff body at the downstream position of a circular cylinder. They investigated the wake characteristics of vortex streets at different spacing ratios. In addition, researchers also have devoted effort to studying the effects of control accessories and surface morphology on FIVs. Cao et al. (2018) used a narrow control element to change the vortex shedding of a transverse vibrating cylinder with the 2P pattern mode and obtained 2S, P+S, and six new vortex shedding modes. Carvalho et al. (2021) arranged several small cylinders around the main cylinder and studied the effect of the rotation speed of small cylinders on the vortex shedding of the main cylinder.

In many engineering situations, FIVs often cause damage to structures. However, by designing an energy harvesting configuration, FIV energy can be converted into electricity to power small electronic devices. Therefore, FIV energy harvesting has received widespread attention worldwide (Gong et al., 2019; Meng et al., 2021). Zhu et al. (2019) studied the vibrational response and EH performance of a cylinder mounted with a Bach-type turbine. They revealed that the projection diameter of the turbine significantly affects the vibrational and rotational responses of the device. The rotational motion of the structure can greatly influence the evolution of the wake street and the oscillation trajectory. Traditional VIV energy harvesting mainly aims at circular cylinders. For VIV energy harvesting using bluff bodies with different cross-sectional shapes, Wang et al. (2018) established a new VIV piezoelectric energy harvester (PEH) model, which can accurately predict the voltage-time history curve from the initial position to the threshold of the lock-in region. Zhao et al. (2020b) proposed a configuration with grooves added to the bluff body to enhance FIV. The results showed that when two grooves are distributed at 60°, galloping will occur, and the energy harvesting performance will be improved. Tang et al. (2022) developed hydroelastic energy harvesters based on the metamaterial design concept. The effect of the number of interfering circular cylinders was analyzed to determine the optimal arrangement of the periodic metamaterial. Wang et al. (2020b) added cylindrical attachments on a bluff body to make the vibration enter the transition region of galloping after the upper branch, thereby enhancing the VIV amplitude and energy harvesting performance. In addition, by using flexible structures, researchers have explored the feasibility of coupling piezoelectric flags and wakes for EH. Latif et al. (2021) placed an inverted C-shaped cylinder in a uniform flow to generate a shedding wake. They found that an inverted C-shaped cylinder influences the EH performance of a piezoelectric flag. In the FIV simulations, researchers usually simplify the model to reduce the amount of computing resources. Ding et al. (2013) applied the two-dimensional URANS equation to simulate the flow-induced motion of a tandem cylinder. The experimental results show that the simulated amplitude and frequency are in good agreement with the experimental results. On one hand, FIV-based EH has been extensively studied in laboratories. On the other hand, researchers and industrialists have also explored its practical applications. For instance, Vortex Hydro Energy has collaborated with the Marine Renewable Energy Laboratory and TAUW to deploy prototypes in the St. Clair River and canals in the Netherlands for harvesting energy from flow-induced motions in rivers (Bernitsas, 2016).

According to the literature review, many studies have been conducted on investigating the FIV phenomenon and FIV-based energy harvesting. The shear layers separated from a bluff body at different $Re$ will form different vortex shedding modes, such as "2S", and "P+S" shedding patterns, and different vortex shedding patterns may affect the performance of FIV energy harvesters (Wang et al., 2021a). Compared with these bluff bodies, the opening angle of the C-shaped bluff body also affects the vortex-shedding behavior. However, the influence on the EH performance is still unclear. Inspired by previous research, this work utilized the wake generated by an inverted C-shaped bluff body to enhance the EH performance of the downstream cylinder. The inverted C-shaped bluff body and the EH-cylinder are arranged in tandem. By changing the angle of the inverted C-shaped bluff body and the distance between the inverted C-shaped bluff body and the EH-cylinder, the hydrodynamic characteristics and EH performance under different conditions are evaluated.

## 2 Mathematical models and governing equations

### 2.1 Hydrodynamic equations

The main objective of this paper is to analyze the WIV phenomenon at high Reynolds numbers and its potential application for EH. The fluid is assumed to be incompressible and viscous. To solve the WIV of an inverted C-shaped bluff body, the two-dimensional URANS equation and SST $k-\omega$ turbulence model are used to simulate the fluid flow. The URANS equation consists of the mass and momentum conservation equations, and the specific equations can be written in the following form (Wang et al., 2020a; Zhu et al., 2017):

$$\frac{\partial \overline{u_i}}{\partial x_i}=0; \tag{1}$$

$$\frac{\partial \rho \overline{u_i}}{\partial t}+\frac{\overline{u_i u_j}}{\partial x_j}=-\frac{\partial \overline{p}}{\partial x_i}+\mu \nabla^2 \overline{u_i}-\frac{\partial \rho \bar{u}_i' \bar{u}_j'}{\partial x_j}, \tag{2}$$

where $-\rho \bar{u}_i' \bar{u}_j'$ is the Reynolds stress and is defined as:

$$-\rho \bar{u}_i' \bar{u}_j'=\mu_{\mathrm{t}}\left(\frac{\partial u_i}{\partial x_j}+\frac{\partial u_j}{\partial x_i}\right)-\frac{2}{3}\rho k_{\mathrm{t}} \delta_{ij}. \tag{3}$$

In the above equations, $t$, $p$, and $\rho$ denote the time, pressure, and fluid density, respectively, and $\overline{u_i}$ and $\bar{u}_i'$ represent the mean values of the Cartesian velocity and fluctuation velocity, respectively. $k_{\mathrm{t}}$ and $\delta_{ij}$ are the kinetic energy of turbulence and the Kronecker delta function, respectively. $\mu$ and $\mu_{\mathrm{t}}$ are the dynamic viscosity and the turbulent viscosity, respectively.

Considering the superior performance of the SST $k-\omega$ turbulence model in calculating the vortex characteristics of the flow field, this model is used to solve the fluid–structure interaction issue in this work. The two equations for the turbulent kinetic energy ($k_{\mathrm{t}}$) and specific dissipation rate ($\omega$) in SST $k-\omega$ are as follows (Zhu et al., 2018):

$$\frac{\partial(\rho k_{\mathrm{t}})}{\partial t}+\frac{\partial(\rho k_{\mathrm{t}} u_i)}{\partial x_i}=\frac{\partial}{\partial x_j}\left[\left(\mu+\frac{\mu_{\mathrm{t}}}{\sigma_k}\right)\frac{\partial k_{\mathrm{t}}}{\partial x_j}\right]+\tilde{Q}_k-\beta^* \rho \omega k_{\mathrm{t}}; \tag{4}$$

$$\frac{\partial(\rho \omega)}{\partial t}+\frac{\partial(\rho \omega u_i)}{\partial x_i}=\frac{\partial}{\partial x_j}\left[\left(\mu+\frac{\mu_{\mathrm{t}}}{\sigma_\omega}\right)\frac{\partial \omega}{\partial x_j}\right]+ Q_\omega-\beta \rho \omega^2+2\rho \frac{(1-T_1)}{\omega \sigma_{\omega,2}}\frac{\partial k_{\mathrm{t}}}{\partial x_j}\frac{\partial \omega}{\partial x_j}. \tag{5}$$

In Eqs. (4) and (5):

$$\tilde{Q}_k=\min(Q_k, 10\beta^* \rho k_{\mathrm{t}} \omega); \tag{6}$$

$$Q_k=2\mu_{\mathrm{t}} S_{ij}-\frac{2}{3}\rho k_{\mathrm{t}} \frac{\partial v_i}{\partial x_j}\delta_{ij}; \tag{7}$$

$$Q_\omega=\gamma\left(2\rho R_{ij}\cdot R_{ij}-\frac{2}{3}\rho \omega \frac{\partial u_i}{\partial x_j}\delta_{ij}\right); \tag{8}$$

$$S_{ij}=0.5\left(\frac{\partial u_i}{\partial x_j}+\frac{\partial u_j}{\partial x_i}\right), \tag{9}$$

where $\tilde{Q}_k$ and $Q_k$ are the effective rate and the production rate of $k_{\mathrm{t}}$ due to the average velocity gradient, respectively. $Q_\omega$ is the production rate of $\omega$. $R_{ij}$ is the mean rate of the deformation component, and $\sigma_k$, $\sigma_\omega$, $\beta$ and $\gamma$ are model coefficients evaluated by Yu and Thé (2016):

$$\varphi=\varphi_1 T_1+\varphi_2(1-T_1). \tag{10}$$

In Eq. (10), $\varphi \equiv \sigma_k$, $\sigma_\omega$, $\beta$ or $\gamma$, and the subscripts 1 and 2 of $\varphi$ indicate the SST $k-\omega$ model and the standard $k-\varepsilon$ model, respectively. The constants and the blending function $T_1$ can be found in Menter ( 1993).

This work uses the FLUENT simulation platform to analyze the characteristics of WIV and overset grid technology to address the dynamic grid problem of oscillating cylinder. The UDF (user defined function) developed based on the fourth-order Runge−Kutta method is used to update the mesh during the motion of the vibrating cylinder. The calculation result of each time step in the simulation is used as the initial condition for the next time step. The fourth-order Runge−Kutta method is used to solve the dynamic equations. The flowchart of the numerical simulation process is shown in Fig. 1.

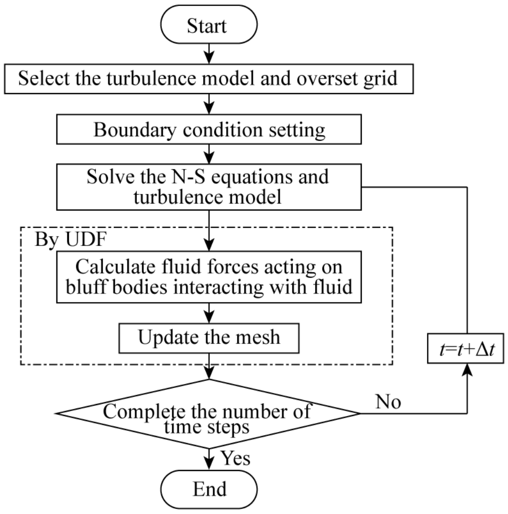

**Fig. 1.** Flowchart of the simulation process.

### 2.2 Dynamical modeling of the coupled system

The WIV of the inverted C-shaped bluff body studied in this work is a typical FIV phenomenon. A static inverted C-shaped bluff body and a vibrating cylinder with single-degree-of-freedom (SDOF) are set up in the flow field. The classical "Mass-Damper-Spring" oscillator model is used to describe the dynamic characteristics of the EH-cylinder. The SDOF oscillating cylinder is modeled by a second-order ordinary differential equation (ODE) as follows:

$$M\ddot{y}+C\dot{y}+Ky=F_{\mathrm{fluid},y}(t), \tag{11}$$

where $M$, $C$, and $K$ represent the total mass, the system damping, and the system stiffness, respectively. $y$ is the displacement of the cylinder, and $F_{\mathrm{fluid},y}$ denotes the fluid force acting on the cylinder in the $y$-direction. During the vibration of the cylinder, a certain volume of surrounding fluid moves along the cylinder. This effectively adds some inertia to the system. Therefore, the added mass effect must be taken into account. The added mass ($m_{\rm a}=C_{\rm a}m_{\rm d}$) can be estimated by the added mass factor ($C_{\rm a}$) and the displaced mass of fluid ($m_{\rm d}$). Note that the additional mass is taken into account in the fluid force term.

The total system power is calculated over one vibration period and is defined as (Zhang et al., 2018a):

$$P_{\rm out}=\frac{1}{T_{\rm osc}}\int_0^{T_{\rm osc}}F_{{\rm fluid},y}\dot{y}{\rm d}t, \tag{12}$$

where $T_{\rm osc}$ represents the vibration period of the oscillating cylinder.

Substituting Eq. (11) into Eq. (12), one can obtain

$$P_{\rm out}=\frac{1}{T_{\rm osc}}\int_0^{T_{\rm osc}}(M\ddot{y}+C\dot{y}+Ky)\dot{y}{\rm d}t. \tag{13}$$

According to the literature (Zhang et al., 2018a), the total system power is determined by the damping term. Thus, Eq. (13) can be simplified as follows:

$$P_{\rm out}=\frac{1}{T_{\rm osc}}\int_0^{T_{\rm osc}}C\dot{y}^2{\rm d}t. \tag{14}$$

As stated in Eq. (11), the damping ($C$) represents the total damping of the system, including the dissipated damping ($C_{\rm diss}$) and energy harvesting-induced ($C_{\rm harness}$) damping. The total converted power ($P_{\rm out}$) associated with the total system damping cannot be fully utilized. When evaluating the effective power ($P_{\rm harness}$), it is necessary to subtract the dissipated power ($P_{\rm diss}$). However, the dissipated damping and power are difficult to measure and distinguish in such a multiphysics system. Note that the maximum attainable power ($P_{\rm harness}$) is positively proportional to the dissipated power ($P_{\rm diss}$) (Hu et al., 2022; Liao and Liang, 2018). Therefore, this paper uses the total power to indicate the EH performance, as described in the literature (Han et al., 2020; Zhang et al., 2018b).

According to the Bernoulli equation, the power input from the flow can be written as:

$$P_{\rm F}=\frac{1}{2}\rho U^3(2A+D)L, \tag{15}$$

where $L$ represents the cylinder length, $U$ stands for the incoming flow velocity, and $D$ is the cylinder diameter.

Finally, the energy harvesting conversion efficiency $\eta$ is calculated as follows:

$$\eta=\frac{P_{\rm out}}{P_{\rm F}\times L_{\rm Betz}}, \tag{16}$$

where $L_{\rm Betz}$ is the theoretical maximum energy extraction efficiency from the flow. The critical value is 59.26% (16/27).

## 3 Physical model and numerical validation

### 3.1 Physical model

Fig. 2 shows a schematic diagram of the WIV EH system proposed in this work. The size of the entire flow region is $35D\times20D$ (length×width), in which $D$ is the diameter of the EH bluff body, i.e., EH-cylinder. The distance between the center of the EH-cylinder and the outlet is set as $25D$ to ensure that the vortex can fully develop after shedding from the upstream bluff body. The distances between the center of the EH-cylinder and the two sidewalls are set to $10D$ to eliminate the interference of the flow field boundary layer. In this configuration, a C-shaped bluff body is treated as a static interference bluff body, and the EH-cylinder is equivalent to an SDOF system composed of a spring, a damper, and a mass. The angle of the inverted C-shaped bluff body is marked as $\alpha$, which ranges from 0° to 180°, with $\nabla\alpha=30°$. The spacing between the EH-cylinder and the C-shaped bluff body is marked as $L$, and $2D$, $3D$, and $4D$ are adopted in this study. Considering that system parameters, such as the diameter, natural frequency, and damping ratio, significantly influence dynamic and EH characteristics, the parameters listed in Table 1, of the WIV EH system in this paper are selected by referring to the physical model reported in Zhao et al. (2020b). Due to the complexity of the WIV problem, conducting a comprehensive three-dimensional simulation is highly time-consuming. In such studies, considering the geometric features of the model, two-dimensional simulations can offer reasonable and reliable predictions (Zhu et al., 2016).

In this work, the reduced velocity ($U^*$) is chosen from 2 to 14. The corresponding Reynolds number ranges from $1.51\times10^4$ to $1.07\times10^5$. The inlet boundary condition of the computational domain is set as the velocity inlet, where $u=U_{\rm in}$, and $v=0$; the outlet boundary condition is set as the pressure outlet with ${\rm d}u/{\rm d}x=0$, and ${\rm d}u/{\rm d}x=0$. The gauge

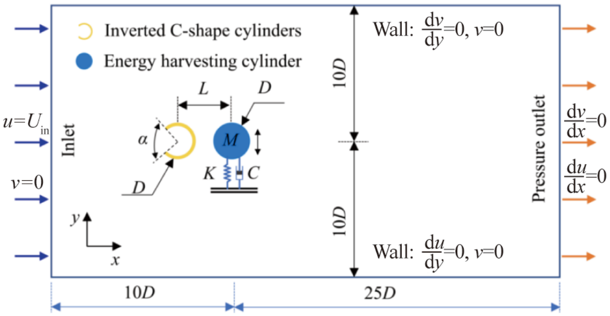

**Fig. 2.** CFD setup for simulating the WIV EH system.

**Table 1** Parameters of the physical model

| Parameter | Value |
|---|---|
| Cylinder diameter $D$ (m) | 0.0889 |
| Cylinder length (m) | 1 |
| Mass $M$ (kg) | 15 |
| Mass ratio $m^*$ | 2.4 |
| Natural frequency $f_{\rm n}$ (Hz) | 0.9641 |
| Damping ratio $\zeta$ | 0.01 |
| Water density $\rho$ (kg/m$^3$) | 998.2 |
| Kinetic viscosity of water $\mu$ (m$^2$/s) | 0.001003 |

pressure is 0, the same as the ambient pressure, and the simulated turbulence intensity is 5%. The upper and lower walls are set as symmetrical.

### 3.2 Computational method validation

This work investigates the EH performance and dynamic response of the WIV of an inverted C-shaped bluff body. A cylinder will exhibit a large amplitude when subjected to fluid forces. When using the overlap mesh method to simulate the motion of an EH-cylinder, large-amplitude mesh deformation can be reasonably avoided, which is significantly beneficial for maintaining high-quality local meshes. The computational domain mesh consists of two parts, namely, the background mesh and the overset mesh, as shown in Fig. 3. The overset grid area is circular and is only applied to the EH-cylinder. The size of the overset grid boundary is set to 3*D*. To accurately determine the flow characteristics of the near-wall surface, the meshes around the inverted C-shaped bluff body and the EH-cylinder are specially refined.

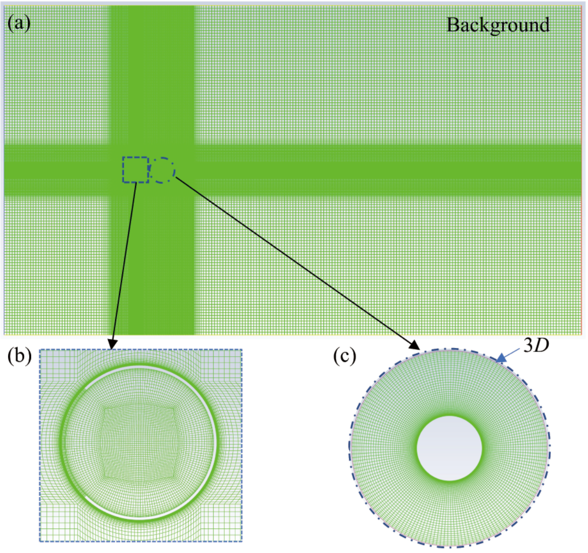

**Fig. 3.** (a) Overall mesh diagram, (b) inverted C-shaped bluff body mesh, and (c) overset mesh.

A reasonable number of grids is crucial for balancing computational efficiency and accuracy. In this work, the effect of $\alpha$ of an inverted C-shaped bluff body on WIV EH was studied. The parameters used for grid independence verification are $U^* = 7$, $L = 2$, and $\alpha = 90°$. Under this condition, the computational model exhibits a large amplitude, which is conducive to independent verification. The four grid groups are named G1, G2, G3, and G4, respectively, and the number of grids increases gradually from G1 to G4. The C-shaped bluff body and the EH-cylinder use the same mesh parameters. The wall $y$+ is a nondimensional spacing that describes the mesh size for a particular flow and is used to determine whether the influence in the adjacent wall is laminar or turbulent, thereby indicating the boundary layer solution. The height of the first layer of the G3 group grid is 0.0019$D$ according to the formula $y^+ = \frac{\rho \Delta y}{\mu}\sqrt{\frac{\tau_{\rm w}}{\rho}}$ (Salim et al., 2010), where $\Delta y$ is the height of the first layer and $\tau_{\rm w}$ is the wall shear stress. The $y^+$ parameters of the four groups of grids are identified as 6.0, 5.7, 5.3, and 5.0, respectively. The overset grid and the background grid use the same $y^+$ parameters. The specific mesh numbers and simulation results are listed in Table 2. When comparing G2 and G3, the changes in the amplitude, RMS lift coefficient, and average drag coefficient are 7.06%, 1.72%, and 4.4%, respectively. The discrepancies between G3 and G4 are 5.29%, 0.54%, and 1.10%, which are all smaller than 5.5%. The results show that the grids of the G3 group can provide sufficient accuracy to capture the flow features, so the grids of the G3 group are selected as the basis mesh for the following research. Fig. 4 shows the time-history curves of the drag and lift coefficients of the G3 mesh group. Affected by the inverted C-shaped bluff body, multiharmonic effects appear in the lift coefficient curve of the EH-cylinder. After the grid independence verification in Table 2, the grid size remains the same in subsequent simulations. The $y^+$ in subsequent simulations will vary, ranging from 1.6 to 10.1.

By abiding by the condition of the G3 group mesh and under the same flow speed $U^* = 7$, different time steps of 0.005, 0.007, and 0.009 s are selected for numerical simulation. The time-history curve of the amplitude is shown in Fig. 5. The simulation converges after 15 s when the time step is 0.005 or 0.007 s. The convergence rates of the two cases are faster than those of the case with a time step of 0.009 s. After 20 s, the amplitudes of the three simulation results are almost the same. Considering the efficiency and the convergence rate, the simulation time step is set as 0.007 s.

After grid independence verification and simulation time step reasonability check, the blockage rate of the simulation model is analyzed under the conditions of G3 mesh at a time step of 0.007 s. In this paper, three verification models, namely, BR1, BR2, and BR3, are established. The specific blockage rate values and simulation results are listed in Table 3. It can be seen that the differences in the amplitude, RMS lift coefficient, and average drag coefficient of

**Table 2** Mesh parameters and results ($U^*$=7, $L$=2, and $\alpha$=90°)

| Grid | Foreground | Background | $y^+$ | $A_{\max}/D$ | $C_{\rm Lrms}$ | $C_{\rm Dmean}$ |
|---|---|---|---|---|---|---|
| G1 | 5576 | 70106 | 6.0 | 1.1174 (–) | 0.3652 (–) | 0.9313 (–) |
| G2 | 6624 | 75380 | 5.7 | 1.1346 (1.54%) | 0.3613 (1.07%) | 0.9141 (1.85%) |
| G3 | 7872 | 80093 | 5.3 | 1.0545 (7.06%) | 0.3675 (1.72%) | 0.9543 (4.4%) |
| G4 | 8820 | 84848 | 5.0 | 1.1103 (5.29%) | 0.3655 (0.54%) | 0.9438 (1.10%) |

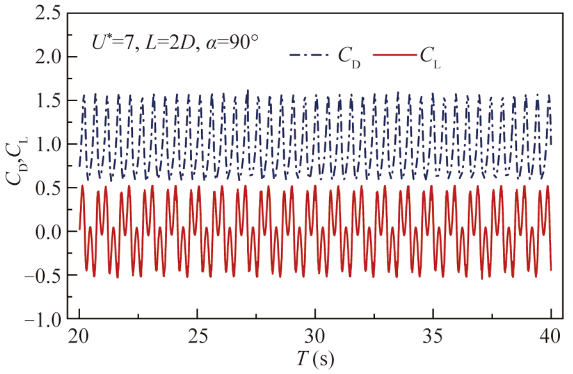

**Fig. 4.** Time-history curves of drag and lift coefficients calculated by using the G3 grid model.

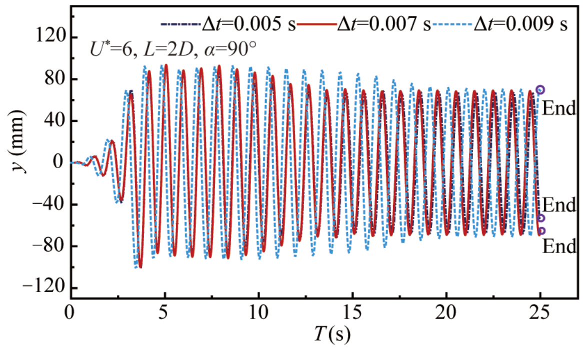

**Fig. 5.** Time-history displacement responses calculated using different time steps.

**Table 3** Sensitivity studies of the blockage ratio

| Blockage ratio | Value | $A_{\max}/D$ | $C_{\mathrm{Lrms}}$ | $C_{\mathrm{Dmean}}$ |
|---|---|---|---|---|
| BR1 | 8% | 1.074 | 0.357 | 1.105 |
| BR2 | 5% | 1.055 (1.8%) | 0.351 (1.7%) | 1.019 (7.8%) |
| BR3 | 2% | 1.051 (0.4%) | 0.350 (0.1%) | 1.002 (1.7%) |

between BR2 and BR1 are 1.8%, 1.7%, and 7.8%, respectively. When the blockage rate is 2.0%, if we compare BR3 and BR2, the differences in the amplitude, RMS lift coefficient, and average drag coefficient are 0.4%, 0.3%, and 1.7%, respectively. The accuracy requirement is met when the blockage rate is 5.0%. Before carrying out the simulation study, the amplitude of the single circular cylinder simulated by the present procedure is further compared with that in previous references (Bernitsas, 2016; Khalak and Williamson, 1999), as shown in Fig. 6. The simulated VIV response of the single cylinder agreed well with the results in the literature (Bernitsas, 2016; Khalak and Williamson, 1999). Overall, the present procedure is reliable and can meet the required accuracy requirements.

## 4 Results and analyses

### 4.1 Vibration characteristics and EH at different angles

### 4.1.1 *Hydrodynamic characteristic analysis*

In this section, the VIV response of a single cylinder is compared with the WIV response of an EH-cylinder under the interference of an inverted C-shaped bluff body. Fig. 7 shows the dimensionless amplitudes and frequency results of the WIV of the EH-cylinder. It can be seen in Fig. 7a that the EH-cylinder has nearly the same vibration characteristics when $\alpha \leqslant 60°$, and the response curves all reach the maximum amplitude when $U^* = 6$. The EH-cylinder reaches the maximum amplitude when $U^* = 7$ and $\alpha \geqslant 120°$. However, the optimal flow velocity for reaching the maximum amplitude increases to $U^* = 8$ when $\alpha = 90°$. Overall, when $L = 2D$, the dimensionless amplitude of the EH-cylinder shows a similar variation trend at different $\alpha$ values: the dimensionless amplitude first increases rapidly, and then gradually decreases with increasing $U^*$. Unlike the VIV of a single cylinder, the WIV of an EH-cylinder has a wider "lock-in" region. Even when $U^* = 14$, the dimensionless amplitude of the EH-cylinder still is still 0.2$D$ at $\alpha = 0°$, and 0.6$D$ at $\alpha = 180°$. The wide "lock-in" region agrees with the WIV of tandem cylinders reported in the literature (Chen et al., 2018). Fig. 7b shows the dimensionless frequency results for the EH-cylinder. It can be seen that there is a significant difference in the frequency characteristics between the EH-cylinder and the single cylinder. The "lock-in" region for the single cylinder is between $U^* = 4$ and $U^* = 12$. Outside of the "lock-in" region, the dimensionless frequency increases sharply, accompanied by a drastic decrease in amplitude to almost 0. However, the EH-cylinder in the wake flow can still vibrate intensely after the oscillation frequency exceeds the natural frequency, which indicates that the definition of the "lock-in" region for a single cylinder becomes unsuitable for the WIV of tandem cylinders. It can be seen in Fig. 7b that when $U^* > 5$, the dimensionless frequency increases almost linearly. The dimensionless frequency increases fastest at $\alpha \leqslant 60°$ and slowest at $\alpha = 180°$. The EH-cylinder can still maintain a large-amplitude vibration even after the oscillation frequency deviates far from the natural frequency. Hence, a wide "soft lock-in" region is formed. The experimental results indicate that an inverted C-shaped bluff body is beneficial for improving energy harvesting performance.

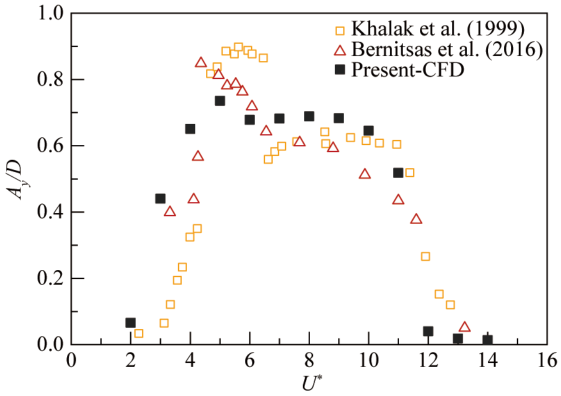

**Fig. 6.** Validation of the numerical model of a single circular cylinder.

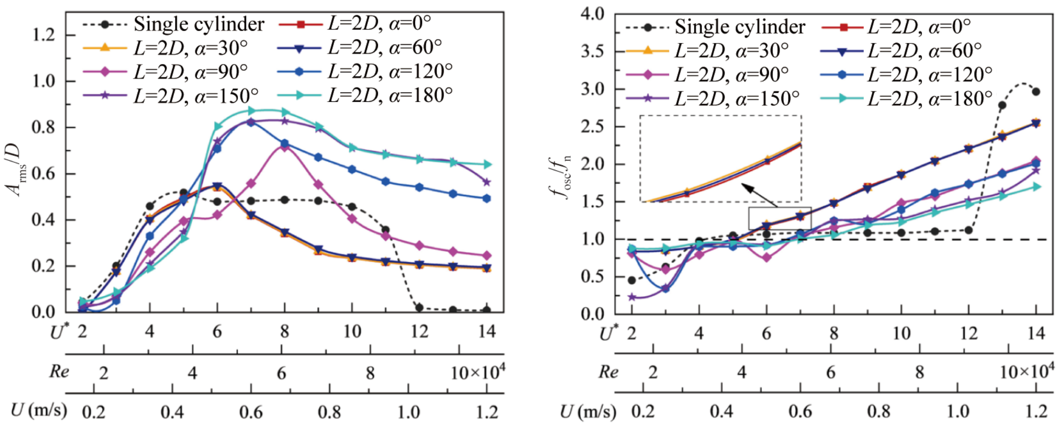

(a) Dimensionless amplitude (b) Dimensionless frequency

**Fig. 7.** Dimensionless amplitude (a) and dimensionless frequency (b) versus the reduced velocity.

The FFT transformations are performed on the time-history displacement responses and lift coefficients to reveal that the EH-cylinder maintains large amplitudes at large $U^*$. The time-history curve and FFT transformation for $U^* = 10$ at different $\alpha$ are shown in Fig. 8. It can be seen from Fig. 8a that the dimensionless amplitude and lift coefficient vary in opposite directions. The main frequency of the lift coefficient is the same as the oscillation frequency of the EH-cylinder and does not match the natural frequency. Generally, the frequency mismatch becomes more evident as the velocity increases. In addition, affected by the wake flow of the inverted C-shaped bluff body, high-order frequency components (e.g., the third-order harmonic component in Fig. 8b) appear in the lift coefficient. When $\alpha = 150°$ and 180°, the amplitude of the third-order frequency component approaches that of the first-order component, and the EH-cylinder can still maintain a high vibration amplitude after deviating from the natural frequency.

Fig. 9 shows the results of the mean drag coefficient ($C_{\mathrm{Dmean}}$) and the RMS lift coefficient ($C_{\mathrm{Lrms}}$). Due to the interference of the wake generated by the inverted C-shaped bluff body, $C_{\mathrm{Dmean}}$ of the EH-cylinder is smaller than that of the single cylinder. Overall, $C_{\mathrm{Dmean}}$ shows a trend of first increasing and then decreasing. Notably, the drag crisis phenomenon occurs at low Reynolds numbers, wherein $C_{\mathrm{Dmean}}$ becomes negative. Additionally, as the angle increases, the Reynolds number range of the negative average drag coefficient appears to expand. At $\alpha = 180°$, the Reynolds number range where a negative $C_{\mathrm{Dmean}}$ occurs is from $1.51\times10^4$ to $3.80\times10^4$. To figure out why the average drag coefficient becomes negative at low $U^*$, the time-averaged pressure coefficient of the EH-cylinder is analyzed.

Fig. 10 depicts the time-averaged pressure coefficient ($C_{\mathrm{Pmean}}$) and the transient pressure coefficient at different time for the EH-cylinder with $\alpha = 150°$. When the average drag coefficient is negative, the time-averaged coefficient of the pressure in front of the EH-cylinder is low, and that in the rear is high. The pressure difference causes negative resistance. The transient pressure coefficient diagram shows that when $U^* = 4$, vortices form in the gap and behind the inverted C-shaped bluff body, and the vortices interact with the front surface of the EH-cylinder. As a result, the pressure on the front surface of the EH-cylinder is lower than that on the rear surface. However, when $U^* = 6$ and the EH-cylinder moves from the middle position to the maximum displacement (from Moment #1 to #2, or #3 to #4*),* the front surface of the EH-cylinder has no contact with the vortex generated by the inverted C-shaped bluff body. Consequently, the higher pressure in front of the EH-cylinder leads to a positive average drag coefficient. When $\alpha = 0°$, 30°, and 60°, a plateau in the RMS lift coefficient is observed at $U^* > 6$, and the RMS lift coefficient gradually decreases with increasing $U^*$. When $\alpha \geqslant 90°$ and $U^* < 8$, the RMS lift coefficient clearly fluctuates due to the interaction between the unsteady wake flow and the EH-cylinder, and the dimensionless amplitude of the EH-cylinder also climbs rapidly to the maximum.

### 4.1.2 *Energy harvesting performance analysis*

Fig. 11 shows the surface and contour plots of the output power at different angles when the spacing $L$ is $2D$. It can be seen that a higher power output can be obtained in the intersection region with an angle ranging from 90° to 180° and a reduced velocity ranging from 6 to 14. It means that the power output is greatly affected by the angle: a larger angle can lead to a higher power output. The black dashed line in Fig. 11b indicates that the maximum output power is achieved under specific conditions. When the distance $L$ is $2D$, and the angle and reduced velocity are on the black dashed line, the energy harvester can produce the maximum power output. As shown in the surface plot and contour plot, there are two power peaks at an angle of 150°, appearing at the reduced velocities of 8 and 14, respectively. The EH performance is improved when the angle is 150°, as indicated by the dotted line in Fig. 11b. It should be noted that the dimensionless amplitudes at 150° and 180° are similar.

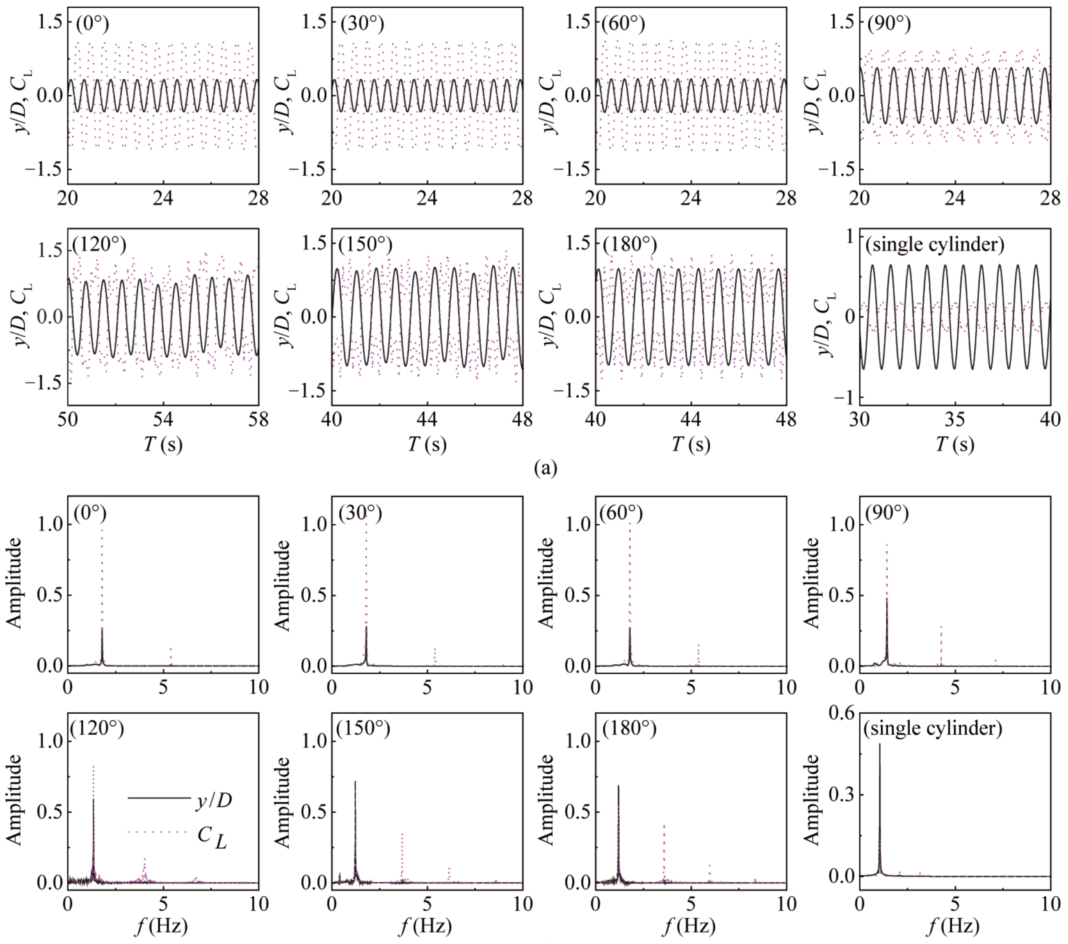

(a)

(b)

**Fig. 8.** (a) Time history vibration amplitudes and lift coefficient of the EH-cylinder, and (b) FFT transformation at $U^*$=10 and $L = 2D$.

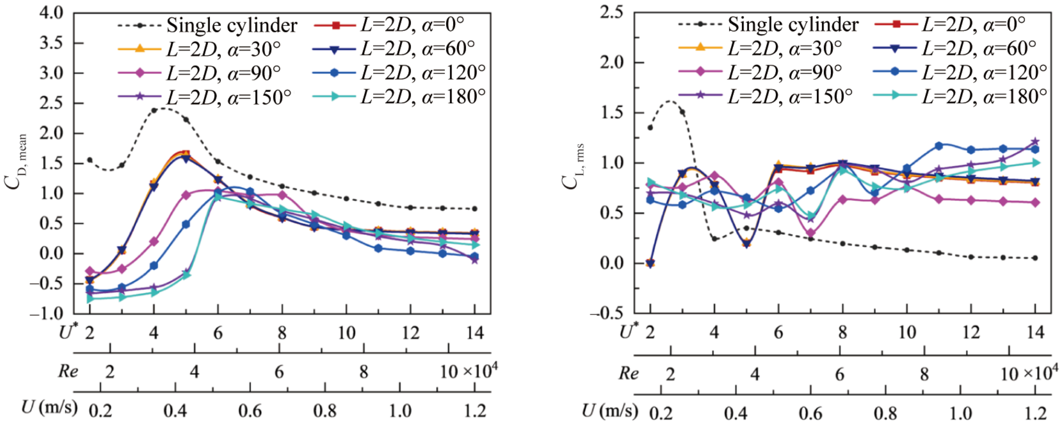

(a) Average drag coefficient

(b) RMS lift coefficient

**Fig. 9.** (a) Average drag coefficient, and (b) RMS lift coefficient versus the reduced velocity.

However, the dimensionless frequency at 150° is higher, corresponding to better EH performance.

## 4.2 Vibration characteristics and EH at different spacings

### 4.2.1 *Vibration characteristics analysis*

This section will investigate the influence of the distance $L$ on the vibration characteristics and EH performance, given that the angle is fixed at 150°. Fig. 12 shows the dimensionless amplitude and frequency results for different spacings $L$. When $L$ is $3D$ or $4D$, different response patterns are observed for the EH-cylinder, referred to as combined WIV andWG (Bokaian and Geoola, 1984). Based on the vibration characteristics, the amplitude curve can be catego-

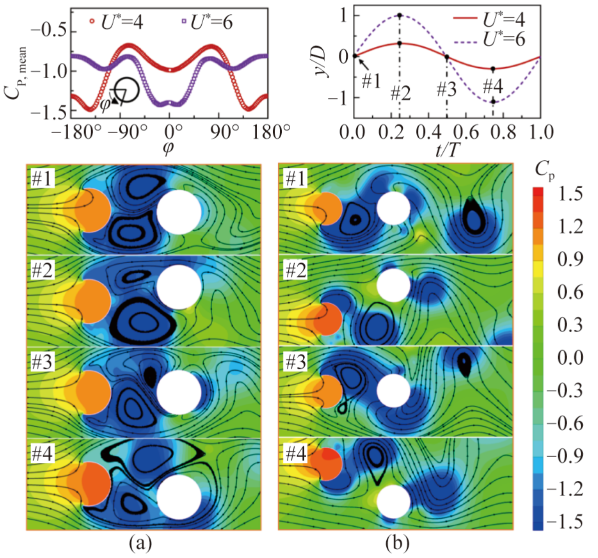

**Fig. 10.** (a) Time-averaged pressure coefficient, (b) time history *y/D*, and transient pressure coefficient of $U^*=4$ (c), and $U^*=6$ (d) for $\alpha=150°$.

rized into three modes: the WIV, the WG, and the transition mode from WIV to WG (WIV-WG for short). The WIV response occurs in the reduced velocity range from 2 to 9, with the dimensionless amplitude decreasing after reaching a maximum at $U^*=8$. The dimensionless frequency enters the "lock-in" region at $U^*=6$, and the frequency characteristics of the WIV mode are the same as those observed at $L=2D$. The WG-type response occurs at a largely reduced velocity from 10 to 14, with the dimensionless amplitude gradually increasing with $U^*$, and the dimensionless frequency remains constant. The WIV-WG response appears at the moderate reduced velocities ranging from 9 to 10. Over this range, the dimensionless frequency decreases from 1.25 to approximately 1. The mode transition is attributed to the sticking effect of the shear layer separated from the C-shaped bluff body to the EH-cylinder and the nonuniform flow in the gap.

Fig. 13 shows the results of the average drag coefficient and the RMS lift coefficient at different *L* values. It can be seen that the average drag coefficient shows the same trend when the spacing is 3*D* and 4*D*. It is worth noting that the average drag coefficient is negative when $U^*$ is smaller than 3. Initially, the average drag coefficient increases with increasing reduced velocity and reaches a maximum when the reduced velocity is 7. The maximum value for $L$=3$D$ is 0.93 and becomes 1.01 when $L$=4$D$. The average drag coefficient then decreases with increasing reduced velocity. When the distance *L* is 3*D* or 4*D*, the RMS lift coefficients exhibit the same evolution trend: the RMS lift coefficient first decreases and then increases, followed by a slow rate of decrease. When $U^*$ is 6, the lift coefficient drops to a minimum value. In the WIV-WG and WG regions, the average drag

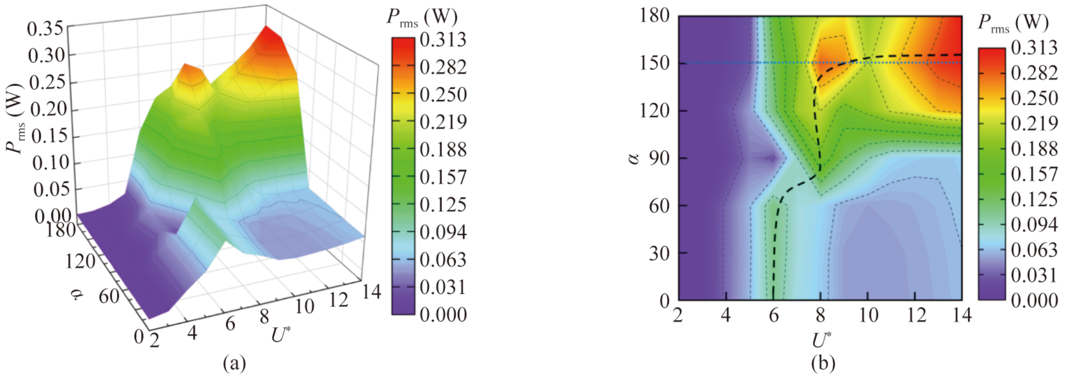

**Fig. 11.** Surface plot and contour plot of the power output generated by the vibrating cylinder energy harvester.

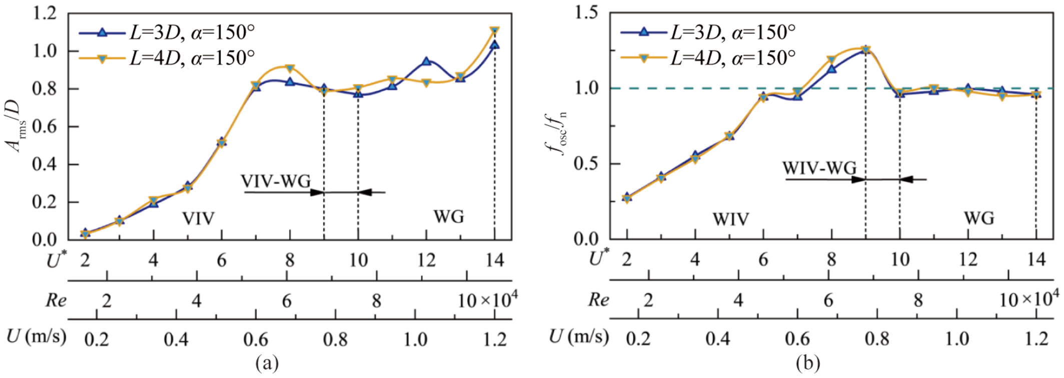

**Fig. 12.** (a) Dimensionless amplitude and (b) dimensionless frequency diagrams for the WIV of the inverted C-shaped interference bluff body.

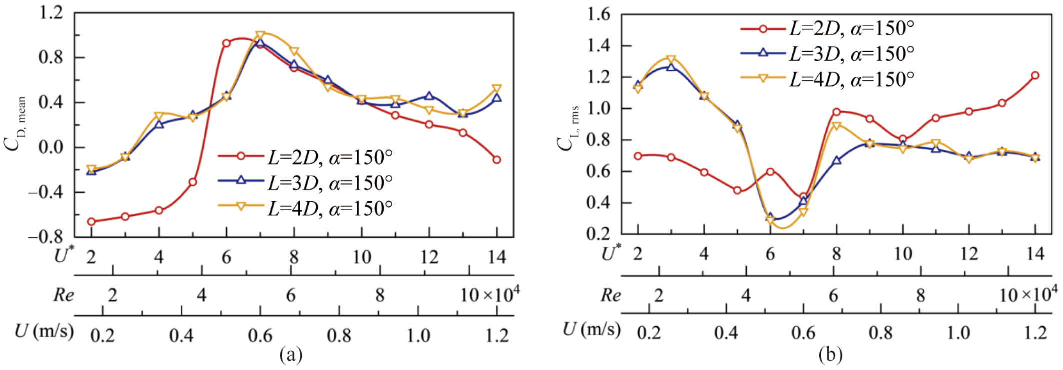

(a) (b)

**Fig. 13.** Results for the (a) average drag coefficient and (b) RMS lift coefficient.

coefficient at $L$ = 3$D$ and 4$D$ is larger than that at $L$ = 2$D$, while the RMS lift coefficient is smaller.

Vortex structure analysis is a useful way to understand FIV. Fig. 14 shows the vorticity plot at a reduced velocity of 8 and $\alpha$ = 150° for spacings of 2$D$ and 4$D$, respectively. It can be seen that the vortex shedding patterns at the two spacings are both “2S”. When the spacing $L$ = 2$D$, the positive vortex (red) sheds from the inverted C-shaped bluff body and moves to the EH-cylinder, surrounding it. When the EH-cylinder moves to the maximum positive displacement, the positive vortex shed from the inverted C-shaped bluff body fuses with the shear layer generated by the EH-cylinder, and the negative vortex (blue) on the EH-cylinder sheds off. Interestingly, the vortex shedding pattern at a distance of $L$ = 4$D$ is the same as that at $L$ = 2$D$. The difference is that the EH-cylinder is not surrounded by vortices at the middle position, which results in nonsynchronization between the vortex motion and the cylinder motion. This change results in different wake disturbance enhancement effects.

Fig. 15 shows the vorticity diagram at a reduced velocity of 14 for spacings of 2$D$ and 4$D$ when $\alpha$ = 150°, respectively. It can be seen that when $L$ = 2$D$, the vortex shedding pattern at $U^*$ = 8 exhibits the “2S” pattern. At the equilibrium position, the vortex between the inverted C-shaped bluff body and the EH-cylinder is tighter at $U^*$ = 14, which results in a smaller amplitude. The vortex shedding mode becomes more complex for a distance of $L$ = 4$D$ and a reduced velocity of $U^*$=14. At the initial equilibrium position (T1), two vortices (V1 and V2) are formed behind the EH-cylinder, and one vortex (V3) is in front of the EH-cylinder. When the EH-cylinder moves to the maximum positive displacement, V1 and V2 shed off, and V3 shed off after fusing with the EH-cylinder. The vortex U1 directly sheds off from the inverted C-shaped bluff body. After $T_2$, the EH-cylinder collides and fuses with a negative vortex at T3 during the movement in the negative direction. As the EH-cylinder moves from the maximum negative displacement (T4) to the equilibrium position, the vortices V4, V5, and V6 successively shed off. The shedding process indicates that the vortex shedding pattern is “2T”, leading to a larger vibration amplitude of the EH-cylinder.

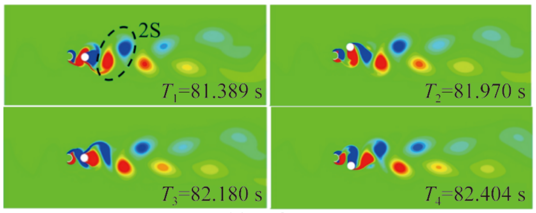

(a) $L$=2$D$

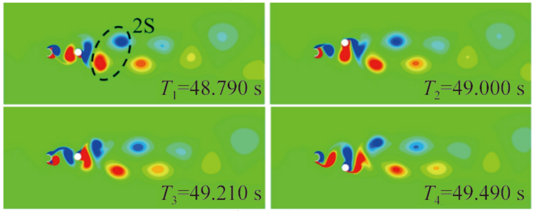

(b) $L$=4$D$

**Fig. 14.** Vortex shedding pattern at $\alpha$ = 150° and $U^*$ = 8.

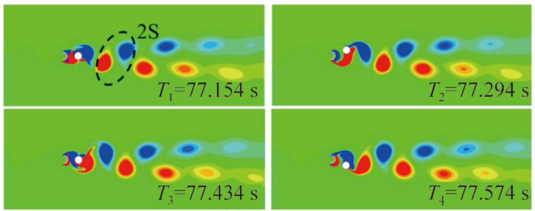

(a) $L$=2$D$

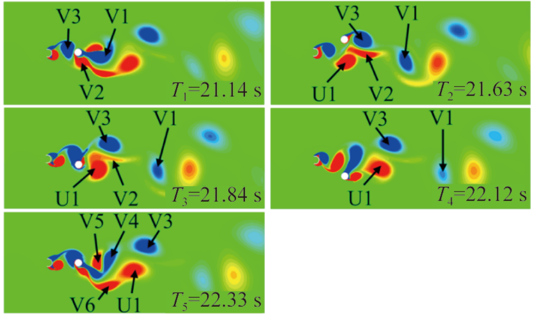

(b) $L$=4$D$

**Fig. 15.** Vortex shedding pattern at $\alpha$ = 150° and $U^*$ = 14.

### 4.2.2 *EH power performance*

Fig. 16 shows the harvested power outputs for different spacings at an angle of 150°. It can be seen that the variation

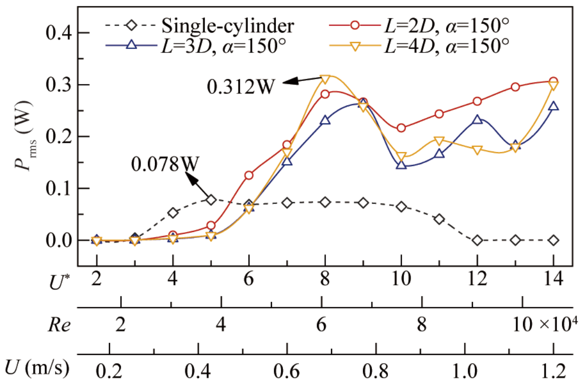

**Fig. 16.** Harvested power outputs at different spacings.

trends of the harvested power curves under different spacings are roughly the same, but there are apparent differences in the harvested power values. The maximum power (0.312 W) occurs at $L = 4D$ and $U^* = 8$. Compared with that of the single cylinder, the harvested power increases by 300%. When $U^*$ is smaller than 7, a larger power output can be obtained when the spacing is $2D$. On the other hand, when $U^*$ is within the velocity range of 10−13, the power outputs for $L = 3D$ and $L = 4D$ are significantly smaller than that for $L = 2D$. The above analysis indicates that the proposed energy harvesting system performs considerably well with a spacing of $L = 2D$.

The energy conversion efficiencies under different conditions (for different $L$ and $\alpha$) are calculated, and the results are shown in Fig. 17. It can be seen that when $L = 2D$, $U^* = 4$, and $\alpha$ is smaller than 60°, the system's energy conversion efficiency reaches a maximum at the beginning of the lock-in region. When $L = 2D$ and $\alpha = 120°$, the system exhibits a stable and optimal EH performance, maintaining a high and relatively constant conversion efficiency over the reduced velocity range from 4 to 7. Moreover, when $\alpha$ exceeds 120°, the maximum efficiencies tend to appear within the reduced velocity range of 6 to 8. When the flow velocity is 2, the EH power of the system is almost minimal, and the efficiency is close to zero. As the velocity increases, according to Eqs. (14)−(15), the harvested power of the system increases, while the input power of the flow is still small. The conversion efficiency gradually increases and reaches a maximum. After that, the system input power increases sharply with velocity, while the increase of the harvested power is limited, and the conversion efficiency gradually decreases and finally stabilizes. Therefore, the overall conversion efficiency of the system first increases, and then decreases with the increase of the reduced velocity.

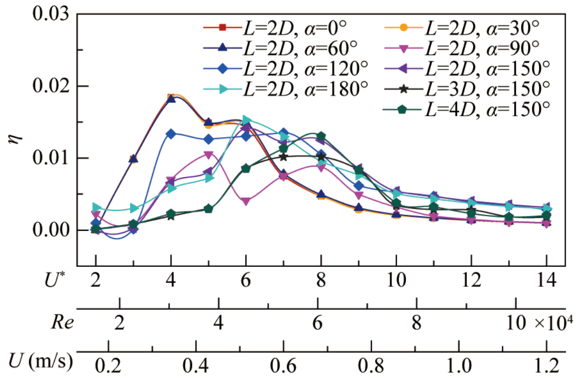

**Fig. 17.** Comparison of the energy conversion efficiencies under different conditions.

## 5 Conclusions

In this paper, an energy harvesting system consisting of an inverted C-shaped bluff body and an EH-cylinder was developed. The inverted C-shaped bluff body is expected to produce an interference wake that can augment the vibration of the EH-cylinder, and thus the power output. The opening angle ($\alpha$) of the inverted C-shaped bluff body and the distance ($L$) between the inverted C-shaped bluff body and the EH-cylinder are the key parameters affecting the hydrodynamics and energy harvesting performance of the proposed system. Experimental case studies have been carried out to understand their effects. Under test conditions, the Reynolds number was controlled from 15100 to 106200. The results derived from this work are summarized as follows.

(1) When $L = 2D$, the EH-cylinder conducts WIV. The dimensionless frequencies of the EH-cylinder indicate a "soft lock-in", resulting in a wider vibrational bandwidth. For $\alpha > 120°$, the EH-cylinder has a higher vibration amplitude. The EH-cylinder exhibits a combined vibration mode of WIV and WG after increasing the spacing $L$ to $3D$ or $4D$ and setting $\alpha = 150°$. The transition from WIV to WG occurs within the reduced velocity range from 9 to 10.

(2) The pressure difference between the front and rear of the EH-cylinder leads to a negative average drag coefficient for different $\alpha$ and $L$. At $L = 2D$, the Reynolds number range corresponding to negative average drag coefficients expands with increasing $\alpha$. The situation becomes different at $L = 3D$ and $4D$, where the Reynolds number range of the negative mean drag coefficients is small at $\alpha = 150°$.

(3) In the WIV vibration mode and the combined WIV and WG vibration modes, the system exhibits higher EH performance and collects more energy when operating at higher velocity and larger $\alpha$. Setting an inverted C-shaped bluff body with a larger $\alpha$ ($\alpha \geqslant 120°$) is particularly beneficial for improving the system harvesting power. The EH efficiency of the system reaches a maximum when $\alpha$ is smaller than 60° and the EH cylinder enters the "lock-in" region.

## Competing interests

The authors declare no competing interests.

## References

Alam, M.M., 2021. Effects of mass and damping on flow-induced vibration of a cylinder interacting with the wake of another cylinder at high reduced velocities, *Energies*, 14(16), 5148.

Alam, M.M., 2022. A note on flow-induced force measurement of oscillating cylinder by loadcell, *Ocean Engineering*, 245, 110538.

Ali, U., Islam, M., Janajreh, I., Fatt, Y. and Alam, M.M., 2021. Flow-induced vibrations of single and multiple heated circular cylinders: A review, *Energies*, 14(24), 8496.

Bernitsas, M.M., 2016. Harvesting energy by flow included motions, in: Dhanak, M.R. and Xiros, N.I. (eds.), *Springer Handbook of Ocean Engineering*, Springer,Cham, 1163–1244.

Bhatt, R. and Alam, M.M., 2018. Vibrations of a square cylinder submerged in a wake, *Journal of Fluid Mechanics*, 853, 301–332.

Bokaian, A. and Geoola, F., 1984. Wake-induced galloping of two interfering circular cylinders, *Journal of Fluid Mechanics*, 146, 383–415.

Cao, M.Y., Jin, H.B. and Shao, C.P., 2018. The single strip-induced change of 2p-mode vortex shedding in the wake of a transversely oscillating cylinder, *Chinese Journal of Theoretical and Applied Mechanics*, 50(4), 734–750. (in Chinese)

Carvalho, I.A., Assi, G.R.S. and Orselli, R.M., 2021. Wake control of a circular cylinder with rotating rods: Numerical simulations for inviscid and viscous flows, *Journal of Fluids and Structures*, 106, 103385.

Chen, W.L., Ji, C.N., Williams, J., Xu, D., Yang, L.H. and Cui, Y.T., 2018. Vortex-induced vibrations of three tandem cylinders in laminar cross-flow: Vibration response and galloping mechanism, *Journal of Fluids and Structures*, 78, 215–238.

Chitrakar, S., Solemslie, B.W., Neopane, H.P. and Dahlhaug, O.G., 2020. Review on numerical techniques applied in impulse hydro turbines, *Renewable Energy*, 159, 843–859.

Ding, L., Bernitsas, M.M. and Kim, E.S., 2013. 2-D URANS vs. experiments of flow induced motions of two circular cylinders in tandem with passive turbulence control for 30,000<*Re*<105,000, *Ocean Engineering*, 72, 429–440.

Elahi, H., Eugeni, M., Fune, F., Lampani, L., Mastroddi, F., Paolo Romano, G. and Gaudenzi, P., 2020. Performance evaluation of a piezoelectric energy harvester based on flag-flutter, *Micromachines*, 11(10), 933.

Fan, K.Q., Liu, J., Wei, D.M., Zhang, D.X., Zhang, Y. and Tao, K., 2021. A cantilever-plucked and vibration-driven rotational energy harvester with high electric outputs, *Energy Conversion and Management*, 244, 114504.

Gong, Y., Shan, X.B., Luo, X.W., Pan, J., Xie, T. and Yang, Z.B., 2019. Direction-adaptive energy harvesting with a guide wing under flow-induced oscillations, *Energy*, 187, 115983.

Han, P., Pan, G., Zhang, B.S., Wang, W. and Tian, W.L., 2020. Three-cylinder oscillator under flow: Flow induced vibration and energy harvesting, *Ocean Engineering*, 211, 107619.

Hu, G.B., Lan, C.B., Tang, L.H., Zhou, B. and Yang, Y.W., 2022. Dynamics and power limit analysis of a galloping piezoelectric energy harvester under forced excitation, *Mechanical Systems and Signal Processing*, 168, 108724.

Jiang, X.Y., Zou, H.X. and Zhang, W.M., 2017. Design and analysis of a multi-step piezoelectric energy harvester using buckled beam driven by magnetic excitation, *Energy Conversion and Management*, 145, 129–137.

Khalak, A. and Williamson, C.H.K., 1999. Motions, forces and mode transitions in vortex-induced vibrations at low mass-damping, *Journal of fluids and Structures*, 13(7-8), 813–851.

Latif, U., Uddin, E., Younis, M.Y., Aslam, J., Ali, Z., Sajid, M. and Abdelkefi, A., 2021. Experimental electro-hydrodynamic investigation of flag-based energy harvesting in the wake of inverted C-shape cylinder, *Energy*, 215, 119195.

Li, C.Z., Zhang, X.S., Hu, X.F., Li, W. and You, Y.X., 2018. The study of flow past multiple cylinders at high reynolds numbers, *Journal of Theoretical and Applied Mechanics*, 50(2), 233–243. (in Chinese)

Li, K.W., Liu, C.W., Jiang, S.S. and Chen, Y.G., 2020b. Review on hybrid geothermal and solar power systems, *Journal of Cleaner Production*, 250, 119481.

Li, X.C., Luo, X., Xu, W., Huang, X.Y. and Chen, L., 2020a. Numerical investigation on high damping, high reynolds numbers wake-induced vibrations of cylinders in tandem arrangement, *Journal of Dalian University of Technology*, 60(1), 46–52. (in Chinese)

Liao, Y.B. and Liang, J.R., 2018. Maximum power, optimal load, and impedance analysis of piezoelectric vibration energy harvesters, *Smart Materials and Structures*, 27(7), 075053.

Meng, J.P., Fu, X.W., Yang, C.Q., Zhang, L.A., Yang, X.H. and Song, R.J., 2021. Design and simulation investigation of piezoelectric energy harvester under wake-induced vibration coupling vortex-induced vibration, *Ferroelectrics*, 585(1), 128–138.

Menter, F. 1993. Zonal two equation k-w turbulence models for aerodynamic flows, *23rd Fluid Dynamics, Plasmadynamics*, *and Lasers Conference*, AIAA, Orlando, USA.

Mrope, H.A., Chande Jande, Y. and Kivevele, T.T., 2021. A review on computational fluid dynamics applications in the design and optimization of crossflow hydro turbines, *Journal of Renewable Energy*, 2021, 5570848.

Munir, A., Zhao, M., Wu, H. and Tong, F.F., 2021. Flow-induced vibration of a rotating circular cylinder at high reduced velocities and high rotation rates, *Ocean Engineering*, 238, 109562.

Peng, X.K., Liu, Z.C. and Jiang, D., 2021. A review of multiphase energy conversion in wind power generation, *Renewable and Sustainable Energy Reviews*, 147, 111172.

Qin, B., Alam, M.M. and Zhou, Y., 2017. Two tandem cylinders of different diameters in cross-flow: Flow-induced vibration, *Journal of Fluid Mechanics*, 829, 621–658.

Qin, B., Alam, M.M. and Zhou, Y., 2019. Free vibrations of two tandem elastically mounted cylinders in crossflow, *Journal of Fluid Mechanics*, 861, 349–381.

Salim, S.M., Ariff, M. and Cheah, S.C., 2010. Wall y+ approach for dealing with turbulent flows over a wall mounted cube, *Progress in Computational Fluid Dynamics*, *An International Journal*, 10(5-6), 341–351.

Sun, F.C., 2022. Green energy and intelligent transportation–promoting green and intelligent mobility, *Green Energy and Intelligent Transportation*, 1(1), 100017.

Tang, R.J., Gu, Y.B., Abdelkefi, A., Liu, X.W. and Wang, J.L., 2022. Effect of periodic metamaterial structures with different arrangement patterns on the effectiveness of hydroelastic energy harvesters: Computational investigation, *Ocean Engineering*, 244, 110229.

Tian, Y., Guan, W.H., Li, G., Mehran, K., Tian, J.D. and Xiang, L.J., 2022. A review on foreign object detection for magnetic coupling-based electric vehicle wireless charging, *Green Energy and Intelligent Transportation*, 1(2), 100007.

Wang, J.L., Li, G.P., Zhang, M., Zhao, G.F., Jin, Z.L., Xu, K. and Zhang, Z.E., 2018. Energy harvesting from flow-induced vibration: A lumped parameter model, *Energy Sources*, *Part A*: *Recovery*, *Utilization*, *and Environmental Effects*, 40(24), 2903–2913.

Wang, J.L., Su, Z., Li, H., Ding, L., Zhu, H.J. and Gaidai, O., 2020a. Imposing a wake effect to improve clean marine energy harvesting by flow-induced vibrations, *Ocean Engineering*, 208, 107455.

Wang, J.L., Yurchenko, D., Hu, G.B., Zhao, L.Y., Tang, L.H. and Yang, Y.W., 2021a. Perspectives in flow-induced vibration energy harvesting, *Applied Physics Letters*, 119(10), 100502.

Wang, J.L., Zhao, W., Su, Z., Zhang, G.J., Li, P. and Yurchenko, D., 2020b. Enhancing vortex-induced vibrations of a cylinder with rod attachments for hydrokinetic power generation, *Mechanical Systems and Signal Processing*, 145, 106912.

Wang, S.Y., Liao, W.L., Zhang, Z.H., Liao, Y., Yan, M.J. and Kan, J. W., 2021b. Development of a novel non-contact piezoelectric wind energy harvester excited by vortex-induced vibration, *Energy Conversion and Management*, 235, 113980.

Xu, W.H., Ji, C.N., Sun, H., Ding, W.J. and Bernitsas, M.M., 2019. Flow-induced vibration of two elastically mounted tandem cylinders in cross-flow at subcritical reynolds numbers, *Ocean Engineering*, 173, 375–387.

Yang, K., Abdelkefi, A., Li, X., Mao, Y.C., Dai, L. and Wang, J.L., 2021. Stochastic analysis of a galloping-random wind energy harvesting performance on a buoy platform, *Energy Conversion and Management*, 238, 114174.

Yu, H.S. and Thé, J., 2016. Validation and optimization of *SST k-ω* turbulence model for pollutant dispersion within a building array, *Atmospheric Environment*, 145, 225–238.

Zhang, B.S., Mao, Z.Y., Song, B.W., Ding, W.J. and Tian, W.L., 2018a. Numerical investigation on effect of damping-ratio and mass-ratio on energy harnessing of a square cylinder in FIM, *Energy*, 144, 218–231.

Zhang, B.S., Wang, K.-H., Song, B.W., Mao, Z.Y. and Tian, W.L., 2018b. Numerical investigation on the effect of the cross-sectional aspect ratio of a rectangular cylinder in fim on hydrokinetic energy conversion, *Energy*, 165, 949–964.

Zhang, L.B., Dai, H.L., Abdelkefi, A. and Wang, L., 2019. Experimental investigation of aerodynamic energy harvester with different interference cylinder cross-sections, *Energy*, 167, 970–981.

Zhao, D.L., Hu, X.Y., Tan, T., Yan, Z.M. and Zhang, W.M., 2020a. Piezoelectric galloping energy harvesting enhanced by topological equivalent aerodynamic design, *Energy Conversion and Management*, 222, 113260.

Zhao, G.F., Xu, J.K., Duan, K., Zhang, M., Zhu, H.J. and Wang, J.L., 2020b. Numerical analysis of hydroenergy harvesting from vortex-induced vibrations of a cylinder with groove structures, *Ocean Engineering*, 218, 108219.

Zhao, L.C., Zou, H.X., Yan, G., Liu, F.R., Tan, T., Wei, K.X. and Zhang, W.M., 2019a. Magnetic coupling and flextensional amplification mechanisms for high-robustness ambient wind energy harvesting, *Energy Conversion and Management*, 201, 112166.

Zhao, L.C., Zou, H.X., Yan, G., Liu, F.R., Tan, T., Zhang, W.M., Peng, Z.K. and Meng, G., 2019b. A water-proof magnetically coupled piezoelectric-electromagnetic hybrid wind energy harvester, *Applied Energy*, 239, 735–746.

Zhu, H.J. and Wang, K.N., 2019. Wake adjustment and vortex-induced vibration of a circular cylinder with a C-shaped plate at a low reynolds number of 100, *Physics of Fluids*, 31(10), 103602.

Zhu, H.J., Sun, Z.X. and Gao, Y., 2017. Numerical investigation of vortex-induced vibration of a triple-pipe bundle, *Ocean Engineering*, 142, 204–216.

Zhu, H.J., Zhao, H.N., Yao, J. and Tang, Y.B., 2016. Numerical study on vortex-induced vibration responses of a circular cylinder attached by a free-to-rotate dartlike overlay, *Ocean Engineering*, 112, 195–210.

Zhu, H.J., Zhao, Y. and Hu, J., 2019. Performance of a novel energy harvester for energy self-sufficiency as well as a vortex-induced vibration suppressor, *Journal of Fluids and Structures*, 91, 102736.

Zhu, H.J., Zhao, Y. and Zhou, T.M., 2018. CFD analysis of energy harvesting from flow induced vibration of a circular cylinder with an attached free-to-rotate pentagram impeller, *Applied Energy*, 212, 304–321.

Zou, H.X., Zhang, W.M., Li, W.B., Wei, K.X., Gao, Q.H., Peng, Z.K. and Meng, G., 2017. Design and experimental investigation of a magnetically coupled vibration energy harvester using two inverted piezoelectric cantilever beams for rotational motion, *Energy Conversion and Management*, 148, 1391–1398.